CENTRAL RESEARCH LIBRARY

ORNL-TM-3848

cy. 102

LOCKHEED MARTIN ENERGY RESEARCH LIBRARIES

3 4456 0514926 5

THE BEHAVIOR OF GRAPHITE UNDER BIAXIAL TENSION

W. L. Greenstreet
G. T. Yahr
R. S. Valachovic

OAK RIDGE NATIONAL LABORATORY
CENTRAL RESEARCH LIBRARY
DOCUMENT COLLECTION
LIBRARY LOAN COPY
DO NOT TRANSFER TO ANOTHER PERSON
If you wish someone else to see this document, send in name with document and the library will arrange a loan.
UCN-7969
(3 3-67)

OAK RIDGE NATIONAL LABORATORY
OPERATED BY UNION CARBIDE CORPORATION • FOR THE U.S. ATOMIC ENERGY COMMISSION

This report was prepared as an account of work sponsored by the United States Government. Neither the United States nor the United States Atomic Energy Commission, nor any of their employees, nor any of their contractors, subcontractors, or their employees, makes any warranty, express or implied, or assumes any legal liability or responsibility for the accuracy, completeness or usefulness of any information, apparatus, product or process disclosed, or represents that its use would not infringe privately owned rights.

ORNL-TM-3848

Contract No. W-7405-eng-26

THE BEHAVIOR OF GRAPHITE UNDER BIAXIAL TENSION

W. L. Greenstreet
G. T. Yahr
R. S. Valachovic

JULY 1972

OAK RIDGE NATIONAL LABORATORY
Oak Ridge, Tennessee 37830
operated by
UNION CARBIDE CORPORATION
for the
U.S. ATOMIC ENERGY COMMISSION

LOCKHEED MARTIN ENERGY RESEARCH LIBRARIES

3 4456 0514926 5

CONTENTS

	Page
ABSTRACT	1
INTRODUCTION	1
MATHEMATICAL THEORY	2
TESTS AND TESTING PROCEDURES, GRAPHITITE-G MATERIAL	10
TEST RESULTS, GRAPHITITE-G MATERIAL	21
COMPARISONS OF CALCULATED AND EXPERIMENTAL RESULTS	33
CONCLUSIONS	38
ACKNOWLEDGMENTS	39
REFERENCES	40

THE BEHAVIOR OF GRAPHITE UNDER BIAXIAL TENSION

W. L. Greenstreet
G. T. Yahr
R. S. Valachovic

ABSTRACT

A small-deformation elastic-plastic continuum theory for describing the stress-strain behavior of graphite is examined for specimens under biaxial loading at room temperature. The continuum theory takes into account the anisotropy and plastic compressibility of graphite as well as the continuous nonlinearity of the stress-strain response. The measured strains for thin-walled cylindrical shells loaded by internal pressure are shown to agree very closely with the predictions of the theory for both loading and unloading.

Keywords: graphite, constitutive equations, stress, strain, materials testing, mechanical properties, plasticity, biaxial tests, Graphitite-G.

INTRODUCTION

This report describes the examination of an elastic-plastic continuum theory, which was developed to describe the nonlinear mechanical behavior of artificial graphite. The basis of this examination is a comparison between calculated and experimental results for combined stress conditions. Thin-walled cylinders made from extruded graphite were internally pressurized to provide data on loading and unloading response, and the experimentally obtained stress-strain curves were compared with calculated results.

In the main, the circular cylindrical specimens were made from extruded Graphitite-G tubing. Five specimens of this material were tested, while a single specimen, which was made from a specialty graphite, was also used. In each case, the material exhibited transversely isotropic behavior, with the axis of isotropic symmetry being in the direction of the longitudinal axis of the specimen.

The theory examined is briefly described in the next section. The equations employed in this study were based on approximate, but mathematically the simplest, analogs to the physical behavior postulated in the development of the theory.

The second section describes the tests performed using specimens made from Graphitite-G material. Because of variations in properties associated with this material, special procedures for data collection were used to overcome masking effects caused by variations in properties. The use of these procedures allowed parameters in the constitutive equations to be determined from a combination of uniaxial test results and results obtained directly from the specimens after the combined stress tests were completed.

The third section describes the Graphitite-G test results. Further discussion of the elastic-plastic continuum theory is also given in this section. The fourth section gives comparisons between calculated and experimental results for the Graphitite-G and the specialty graphite specimens.

MATHEMATICAL THEORY

The small-deformation elastic-plastic continuum theory,[1,2,3] which was developed to describe artificial graphite behavior, is summarized, and the stress-strain relations for pressurized thin-walled cylinders are given in this section. In the theory, as in the classical mathematical theory of plasticity, it is postulated that the total symmetric strain tensor, ϵ_{KL}, can be decomposed into elastic and plastic components, that is,

$$\epsilon_{KL} = \epsilon^{e}_{KL} + \epsilon^{P}_{KL} , \qquad (K,L = 1,2,3) \tag{1}$$

where ϵ^{e}_{KL} are the elastic components and ϵ^{P}_{KL} are the plastic components. The elastic strains are given by the generalized Hooke's law

$$\epsilon^{e}_{KL} = s_{KLMN}\, \sigma_{MN} , \tag{2}$$

where $s_{KLMN} = s_{MNKL}$ represents the elastic compliances and $\sigma_{KL} = \sigma_{LK}$ is the stress tensor. Equation (2) can be written in incremental form as

$$d\epsilon^{e}_{KL} = s_{KLMN}\, d\sigma_{MN} \ . \tag{3}$$

Prior to discussing the stress-plastic strain relations, loading, or potential, surface behavior must be considered. In the case of artificial graphite, a yield surface in the classical sense does not exist; that is, there exists no surface which encloses a region of purely elastic response. However, the concept of a loading surface, distinct from a yield surface, can be introduced. As shown in Refs. 1 and 2, the loading surface, or plastic potential surface, for artificial graphite may be expressed by

$$f = \frac{1}{2}\, a_{KLMN}\, \sigma_{KL}\sigma_{MN} = \kappa \ , \tag{4}$$

where the constants a_{KLMN} satisfy the relations $a_{KLMN} = a_{MNKL}$ and κ is a scalar function which depends on the history of loading. Equation (4) represents the simplest mathematical form for describing loading surfaces appropriate to the behavior of graphite. For a more general expression for f, which allows for translation and growth of the loading surfaces, the reader is referred to Refs. 1 and 2.

Equation (4) describes the surface associated with initial or first loading from the stress-free state of a virgin material. Loading reversal occurs when the stress point, which represents the stress state in stress space, moves toward the interior of the current loading surface. As a result of loading reversal, a new surface is generated.

Consider the case in which the stress point has moved along an initial loading path in stress space until a stress state denoted by $\sigma_{KL} = \sigma^{*}_{KL}$ is reached. A reversal of loading at $\sigma_{KL} = \sigma^{*}_{KL}$ will start generating a loading surface given by

$$f_{(1)} = \frac{1}{2}\, a_{KLMN}\, \sigma_{KL_{(1)}}\sigma_{MN_{(1)}} = \kappa_{(1)} \ , \tag{5}$$

where

$$\sigma_{KL_{(1)}} = \sigma_{KL} - \sigma^{*}_{KL} \ . \tag{6}$$

Here σ^*_{KL} represents a pseudovirgin state, and the stress during loading reversal is measured from σ^*_{KL} in the same way as it is measured from the zero state during the first loading of the virgin body.

A new reversal of loading at $\sigma^*_{KL_{(1)}}$ will again start generating a new loading surface, which is given in this case by

$$f_{(2)} = \frac{1}{2} a_{KLMN} \sigma_{KL_{(2)}} \sigma_{MN_{(2)}} = \kappa_{(2)} , \tag{7}$$

where

$$\sigma_{KL_{(2)}} = \sigma_{KL} - \sigma^*_{KL_{(1)}} . \tag{8}$$

This process is repeated for every loading reversal.

Before proceeding with the discussion of the elastic-plastic theory, we shall consider uniaxial loading. In his studies of uniaxial loading of graphite, Jenkins[4] tacitly assumed the validity of the postulate expressed by Eq. (1) and established equations of the following forms for describing stress versus longitudinal strain diagrams from uniaxial tests:

$$\epsilon = A\sigma + B\sigma^2 ; \tag{9}$$

for initial loading,

$$\epsilon - \epsilon_m = A(\sigma - \sigma_m) - cB(\sigma - \sigma_m)^2 \tag{10}$$

for unloading from a maximum stress σ_m with the corresponding strain ϵ_m, and*

$$\epsilon - \epsilon_o = A(\sigma - \sigma_o) + cB(\sigma - \sigma_o)^2 \tag{11}$$

for reloading from σ_o with the corresponding strain ϵ_o when $\sigma \leq \sigma_m$. In Eqs. (9), (10), and (11), $A(=1/E)$ is the elastic compliance, B is a material constant which characterizes the plastic deformation, and c is a constant. E is the elastic modulus.

---

*In his first paper,[4] Jenkins took the specific case $\sigma_o = 0$. In a later paper,[5] illustrations of stress-strain curves are given for stresses both in tension and compression.

Jenkins' development[4] resulted in a value of one-half for c, with the value being independent of orientation with respect to the grain, that is, independent of whether the specimen is oriented in the against-grain or with-grain direction. In addition, this constant does not depend upon whether the specimen is being unloaded or reloaded. Since his equations were shown[4,6,7,8] to give good to exceptional representations of graphite behavior, the plastic strains are taken as quadratic functions of the stresses in the mathematical analog to elastic-plastic behavior used here. However, the results of our investigations show that c does not necessarily take the value of one-half as implied by Jenkins, and it is for this reason that we have included it as an unknown constant in Eqs. (10) and (11).

Following the developments in Refs. 1 and 2, the relation between plastic strain increments and stress increments on first loading is given by

$$d\epsilon^{P}_{KL} = \frac{1}{(2f)^{1/2}} \frac{\partial f}{\partial \sigma_{KL}} \frac{\partial f}{\partial \sigma_{MN}} d\sigma_{MN} \ . \tag{12}$$

The relation for the first loading reversal is

$$d\epsilon^{P}_{KL_{(1)}} = \frac{c}{[2f_{(1)}]^{1/2}} \frac{\partial f_{(1)}}{\partial \sigma_{KL_{(1)}}} \frac{\partial f_{(1)}}{\partial \sigma_{MN_{(1)}}} d\sigma_{MN_{(1)}} \ . \tag{13}$$

Similar expressions apply for successive loading reversals. In Eq. (13), c is the same as the constant c in Eqs. (10) and (11). Further,

$$\epsilon^{P}_{KL_{(1)}} = \epsilon^{P}_{KL} - \epsilon^{P*}_{KL} \ , \tag{14}$$

where ϵ^{P*}_{KL} is the plastic strain existing at the instant of reversal at σ^{*}_{KL}.

The relation between total strain increments and stress increments on first loading is

$$d\epsilon_{KL} = s_{KLMN}\, d\sigma_{MN} + \frac{1}{(2f)^{1/2}} \frac{\partial f}{\partial \sigma_{KL}} \frac{\partial f}{\partial \sigma_{MN}}\, d\sigma_{MN} \ . \tag{15}$$

For the first loading reversal the relation is

$$d\epsilon_{KL_{(1)}} = s_{KLMN}\, d\sigma_{MN_{(1)}} + \frac{c}{[2f_{(1)}]^{1/2}} \frac{\partial f}{\partial \sigma_{KL_{(1)}}} \frac{\partial f}{\partial \sigma_{MN_{(1)}}}\, d\sigma_{MN_{(1)}} \ . \tag{16}$$

Here,

$$d\epsilon_{KL_{(1)}} = d\epsilon_{KL} - d\epsilon^{*}_{KL} \ ,$$

where $d\epsilon^{*}_{KL}$ is the total strain at the instant of loading reversal at σ^{*}_{KL}.

To simplify the ensuing discussion, we use contracted notation in which the stress and strain notations have the following equivalences:

$$\begin{aligned} \sigma_1 &= \sigma_{11} & \sigma_4 &= \sigma_{23} \\ \sigma_2 &= \sigma_{22} & \sigma_5 &= \sigma_{31} \\ \sigma_3 &= \sigma_{33} & \sigma_6 &= \sigma_{12} \end{aligned} \tag{17}$$

and

$$\begin{aligned} \epsilon_1 &= \epsilon_{11} & \epsilon_4 &= 2\epsilon_{23} = \gamma_{23} \\ \epsilon_2 &= \epsilon_{22} & \epsilon_5 &= 2\epsilon_{31} = \gamma_{31} \\ \epsilon_3 &= \epsilon_{33} & \epsilon_6 &= 2\epsilon_{12} = \gamma_{12} \ . \end{aligned} \tag{18}$$

Note that γ_{KL} $(K \neq L)$ are the engineering shear strain components.

As mentioned in the Introduction, the material is assumed to be transversely isotropic, and, throughout the subsequent discussions, the 3-axis is the axis of anisotropic symmetry and the 1- and 2-axes lie within the plane of symmetry.* In contracted notation the constitutive equation, Eq. (15), becomes

---

*1 and 2 are against-grain directions, while 3 is the with-grain direction.

$$d\epsilon_K = s_{KL}\, d\sigma_L + \frac{1}{(2f)^{1/2}} \frac{\partial f}{\partial \sigma_K} \frac{\partial f}{\partial \sigma_L}\, d\sigma_L \,, \quad (K,L = 1,2,3,4,5, \text{ or } 6) \tag{19}$$

and the plastic potential equation, Eq. (4), becomes

$$f = \frac{1}{2}\, a_{KL}\, \sigma_K \sigma_L \,. \tag{20}$$

As stated above, the compliances and the coefficients, or constants, in the plastic potential equation are symmetrical. In contracted notations the symmetry relations become

$$s_{KL} = s_{LK}$$

and

$$a_{KL} = a_{LK} \,.$$

We are now in a position to discuss the constants and their relationships to quantities determined from uniaxial tests. The nonzero compliances and their relationships to the usual elastic constants for a transversely isotropic material are*

$$\begin{aligned}
s_{11} &= s_{22} = \frac{1}{E_{11}} \,, \\
s_{12} &= s_{21} = -\frac{\nu_{12}}{E_{11}} = -\frac{\nu_{21}}{E_{11}} \,, \\
s_{23} &= s_{32} = s_{13} = s_{31} = -\frac{\nu_{13}}{E_{11}} = -\frac{\nu_{31}}{E_{33}} \,, \\
s_{33} &= \frac{1}{E_{33}} \,, \\
s_{44} &= s_{55} = \frac{1}{G_{23}} \,, \\
s_{66} &= 2(s_{11} - s_{12}) = \frac{2(1 + \nu_{12})}{E_{11}} = \frac{1}{G_{12}} \,,
\end{aligned} \tag{21}$$

*See Love[9] or Hearmon.[10]

where

E = Young's modulus,

G = elastic shear modulus,

ν_{MN} = Poisson's ratio; the first subscript indicates the direction of applied stress and the second indicates the direction of induced strain.

Note that the constant A in Eqs. (9), (10), and (11) corresponds to s_{11} ($=s_{22}$) and s_{33}.

Through the use of Ref. 1, the following equations can be written for relating the nonzero a_{KL} to parameters that can be determined from uniaxial test results:

$$a_{11} = a_{22} = (2B_{11})^{2/3} ,$$

$$a_{12} = a_{21} = -\mu_{12}^{p} (2B_{11})^{2/3} ,$$

$$a_{23} = a_{13} = a_{31} = a_{32} = -\mu_{13}^{p} (2B_{11})^{2/3} = -\mu_{31}^{p} (2B_{33})^{2/3} , \qquad (22)$$

$$a_{33} = (2B_{33})^{2/3} ,$$

$$a_{44} = a_{55} = (4B_{23})^{2/3} ,$$

$$a_{66} = 2(a_{11} - a_{12}) = 2(2B_{11})^{2/3} (1 + \mu_{12}^{p}) .$$

Here, B_{11} ($=B_{22}$) is the B value [Eq. (9)] for the against-grain direction, B_{33} is the B value for the with-grain direction, and B_{23} is determined from a shear stress versus shear strain diagram. The μ_{12}^{p}, μ_{13}^{p}, and μ_{31}^{p} are the plastic strain ratios. [Again, the subscripts on μ_{KL}^{p} ($K \neq L$) have the same meanings as those for ν_{KL} ($K \neq L$).]

The constitutive equations giving the axial and circumferential strains are written in expanded form below. These equations will be used in a subsequent section for making comparisons between predictions of this theory and measured strains from the thin-walled cylinders. For initial loading,

$$\epsilon_2 = s_{11}\,(1 - \nu_{13}R)\sigma_2 + \frac{1}{2}\left(1 - \mu_{13}^{p}R\right)\left(1 - 2\mu_{13}^{p}R + \frac{a_{33}}{a_{11}}R^2\right)^{1/2} a_{11}^{3/2}\sigma_2^2 \,, \quad (23)$$

and

$$\epsilon_3 = s_{33}\,(R - \nu_{31})\sigma_2 + \frac{1}{2}\left(\frac{a_{33}}{a_{11}}R - \mu_{13}^{p}\right)\left(1 - 2\mu_{13}^{p}R + \frac{a_{33}}{a_{11}}R^2\right)^{1/2} a_{11}^{3/2}\sigma_2^2 \,, \quad (24)$$

where ϵ_2 is the circumferential strain, ϵ_3 is the axial strain, and

$$R = \frac{\sigma_3}{\sigma_2} = \text{constant}$$

is the axial-to-circumferential stress ratio. The corresponding equations for first load reversal or unloading are

$$\epsilon_{2(1)} = s_{11}\,(1 - \nu_{13}R)\sigma_{2(1)} - \frac{c}{2}\left(1 - \mu_{13}^{p}R\right)\left(1 - 2\mu_{13}^{p}R + \frac{a_{33}}{a_{11}}R^2\right)^{1/2} a_{11}^{3/2}\sigma_{2(1)}^2 \,, \quad (25)$$

and

$$\epsilon_{3(1)} = s_{33}\,(R - \nu_{31})\sigma_{2(1)} - \frac{c}{2}\left(\frac{a_{33}}{a_{11}}R - \mu_{13}^{p}\right)\left(1 - 2\mu_{13}^{p}R + \frac{a_{33}}{a_{11}}R^2\right)^{1/2} a_{11}^{3/2}\sigma_{2(1)}^2 \,. \quad (26)$$

The quantities $\epsilon_{2(1)}$, $\epsilon_{3(1)}$, $\sigma_{2(1)}$, and $\sigma_{3(1)}$ $[=R\sigma_{2(1)}]$ are given by

$$\epsilon_{2(1)} = \epsilon_2 - \epsilon_2^* \,,$$

$$\epsilon_{3(1)} = \epsilon_3 - \epsilon_3^* \,,$$

$$\sigma_{2(1)} = \sigma_2 - \sigma_2^* \,,$$

$$\sigma_{3(1)} = \sigma_3 - \sigma_3^* \,.$$

The stresses σ_2^* and σ_3^* are those associated with the load reversal or unloading point; the strains ϵ_2^* and ϵ_3^* are those that existed at the instant of load reversal. Note that the starred quantities were designated by ϵ_m and σ_m in Eq. (10).

TESTS AND TESTING PROCEDURES, GRAPHITITE-G MATERIAL

In this section we describe the biaxial tests conducted on the thin-walled cylindrical specimens as well as uniaxial tests performed to obtain material property data. The material property data were obtained from uniaxial tests on the cylindrical specimens following acquisition of the biaxial data and from standard tensile specimens. These data were used to determine the parameters for use in Eqs. (23) through (26).

Tests were conducted on five cylindrical specimens of the design shown in Fig. 1. As may be seen from the figure, the gage sections of the cylindrical specimens were 6-in. long, with a 0.092-in. wall thickness, and a mean radius of 0.922 in. The specimens were fabricated from tubes having a 1 1/2 in. inside diameter and a 2 in. outside diameter. Short cylindrical sleeves were machined from 2-in.-inside diameter by 2 3/4-in.-outside diameter tube stock and were glued over each end of 10-in.-long cylinders, which were machined to form the gage sections. The composite structures were then machined to the final specimen configuration. Since the specimens were made from extruded tubing, the longitudinal axes of the specimens were parallel with the with-grain direction of the graphite; the material was isotropic in planes normal to the axes of the cylinders.

Each cylindrical specimen was instrumented on the outside surface with strain gages oriented in the axial and circumferential directions. Type C6-121-A Budd Metalfilm gages with a 0.125-in. gage length were used, and they were mounted in pairs (one axial gage and one circumferential gage) at selected locations. One specimen (no. 1) had two sets mounted 180-deg apart at the center of the gage section, while the remaining four had four pairs mounted at 90-deg intervals around the circumference at the center of the gage section. In addition, pairs of gages were mounted

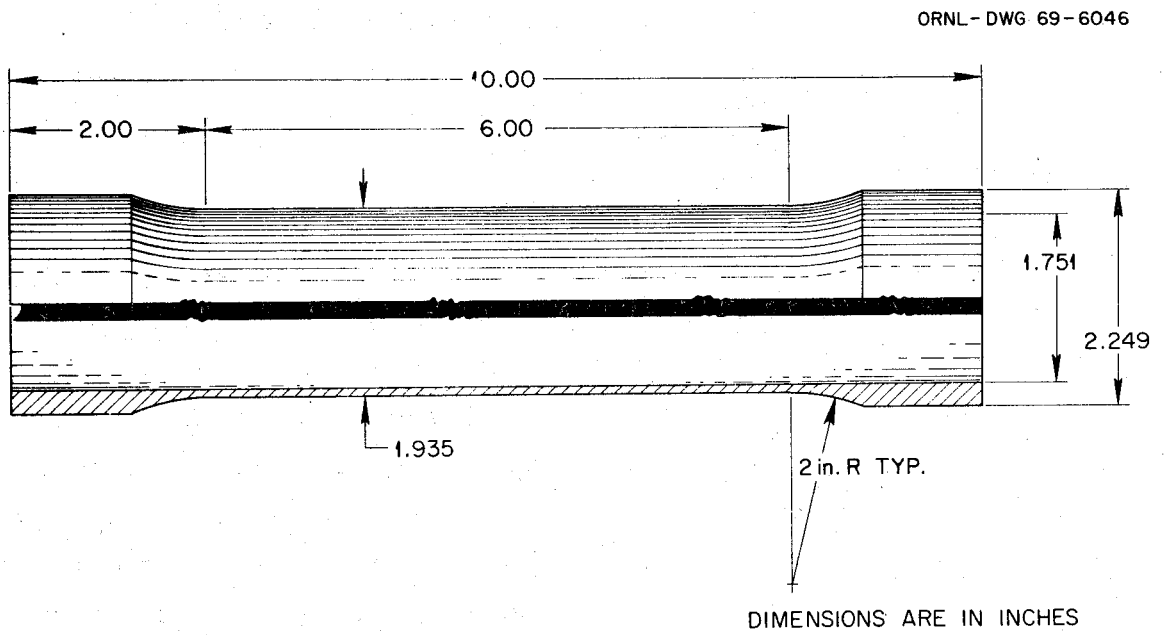

Fig. 1. Design of thin-walled cylindrical specimen.

in the transition regions at the ends of each specimen. In two cases, the specimens (nos. 2 and 3) were extensively strain gaged to obtain strain distributions as functions of axial position.

Figure 2 shows a cylindrical specimen mounted in a loading fixture for applying internal pressure only or an axial tensile force only. A specimen mounted in a loading fixture for applying internal pressure plus a compressive force so that no net axial load is exerted on the specimen is shown in Fig. 3.

Each specimen was subjected to biaxial loading; following this, uniaxial loading conditions were imposed in various sequences. A summary of the tests and test conditions is given in Table 1. The loadings used and the sequences of applications are given in column 2 of the table, where the circumferential to axial stress ratio for each loading is also listed. A cycle consisted of loading to the maximum pressure or load and unloading to zero pressure or load. The specimens were unloaded completely before being subjected to subsequent loadings. The stresses in the axial and circumferential directions for pressure loading were calculated using thin-walled cylinder equations. Note that the sequence of loading is not the same in all cases. Specimen no. 1 was subjected to a maximum internal pressure of 160 psi, while the maximum internal pressure was 200 psi in all other cases. In addition, specimen no. 1 was pressurized to failure under combined stress conditions as a final step. The other specimens were not loaded to failure.

The strains measured at the gage locations along the lengths and around the circumference of specimen nos. 2 and 3 were carefully examined for each of the three types of loading, that is, internal pressure, axial load, and internal pressure with no net axial load. To facilitate this examination, strain distributions were plotted for various load levels. These plots showed that the peak strains which occurred in the transition regions at the ends of the gage section diminished rapidly with distance toward the center of the specimen. Thus, the central regions were not affected by the discontinuity stresses. There were small differences in the strain values measured around the circumferences at the centers of the specimens. As an example of the results obtained, the strains for specimen no. 3 are shown in Fig. 4 for the 200 psi internal pressure

PHOTO 76689

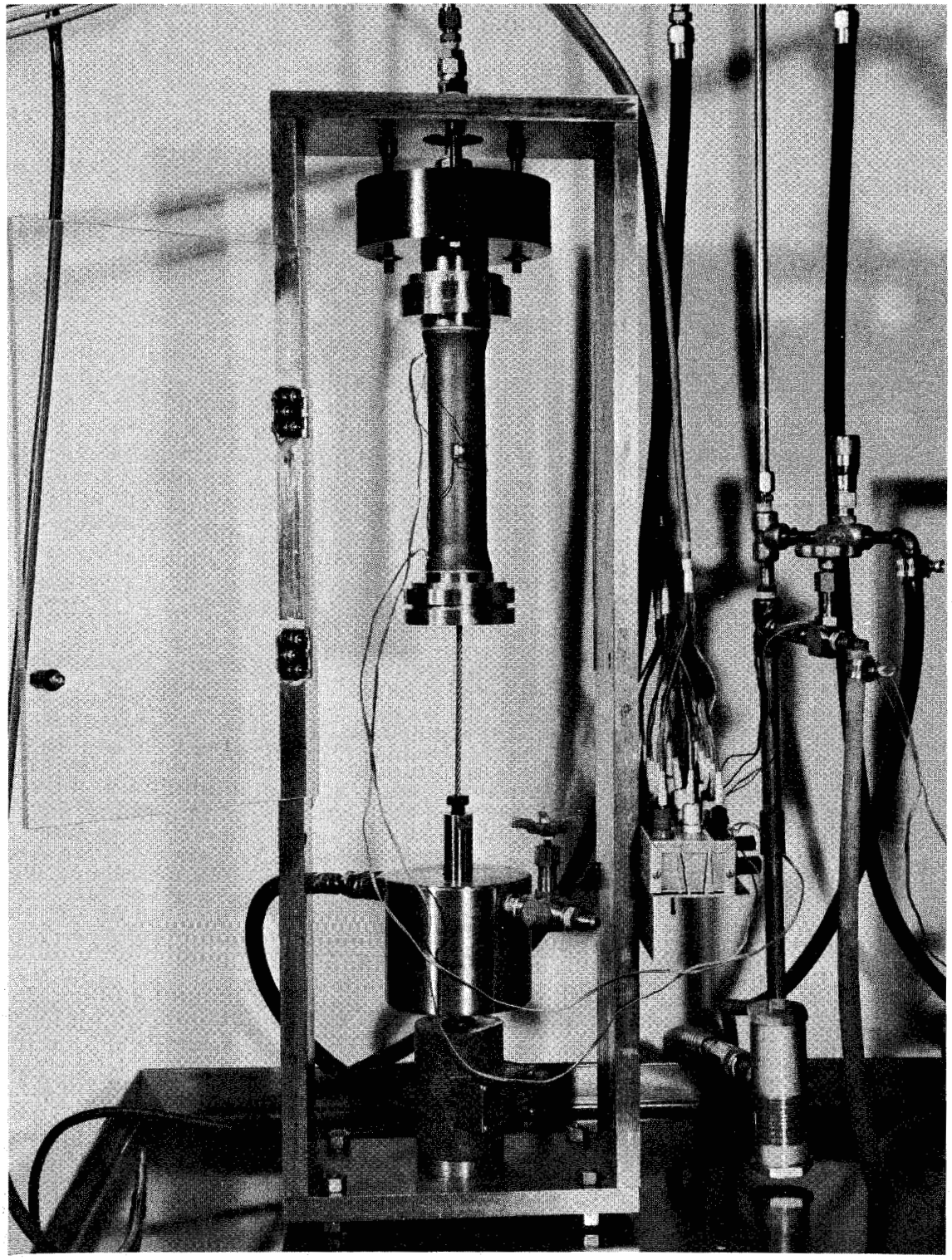

Fig. 2. Cylindrical specimen mounted in internal pressure/axial tension test rig.

PHOTO 76690

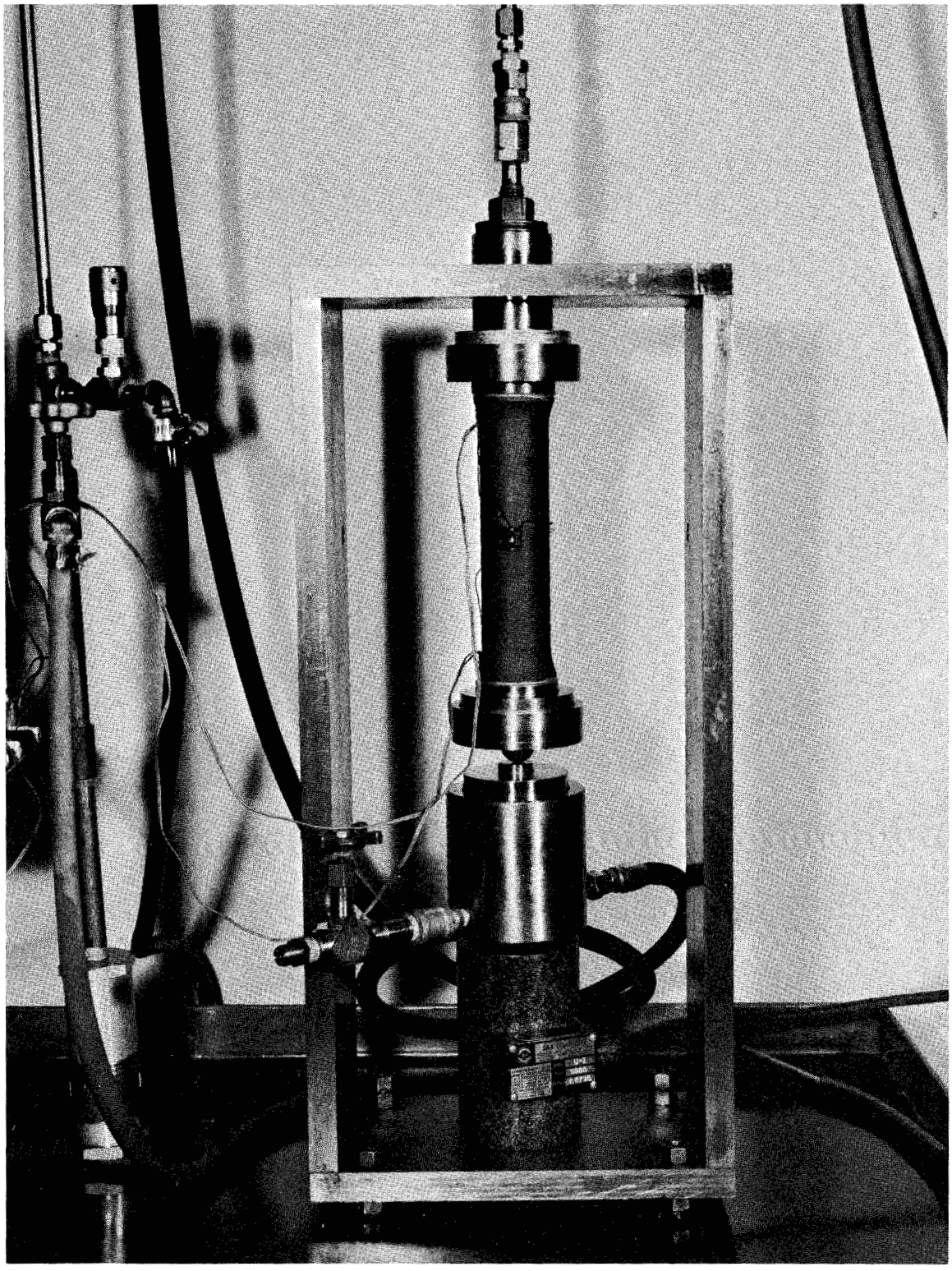

Fig. 3. Cylindrical specimen mounted in internal pressure/axial compression test rig.

Table 1. Outline of tests on Graphitite-G thin-walled cylindrical specimens

Specimen no.	Load type	Maximum internal pressure (psi)	Maximum axial load (lb)	Maximum stress		Number of cycles
				Circumferential (psi)	Axial (psi)	
1	2:1 biaxial	160		1603	802	1
	0:1 axial		900	0	1689	1
	1:0 circumferential	180		1804	0	2
	0:1 axial		1000	0	1877	2
	2:1 biaxial	213		2134	1067	
2	2:1 biaxial	200		2004	1002	1
	1:0 circumferential	190		1904	0	2
	0:1 axial		1000	0	1877	2
3	2:1 biaxial	200		2004	1002	2
	0:1 axial		1000	0	1877	2
	1:0 circumferential	190		1904	0	2
4	2:1 biaxial	200		2004	1002	2
	1:0 circumferential	190		1904	0	2
	0:1 axial		1000	0	1877	2
5	2:1 biaxial	200		2004	1002	2
	1:0 circumferential	190		1904	0	2
	0:1 axial		1000	0	1877	2

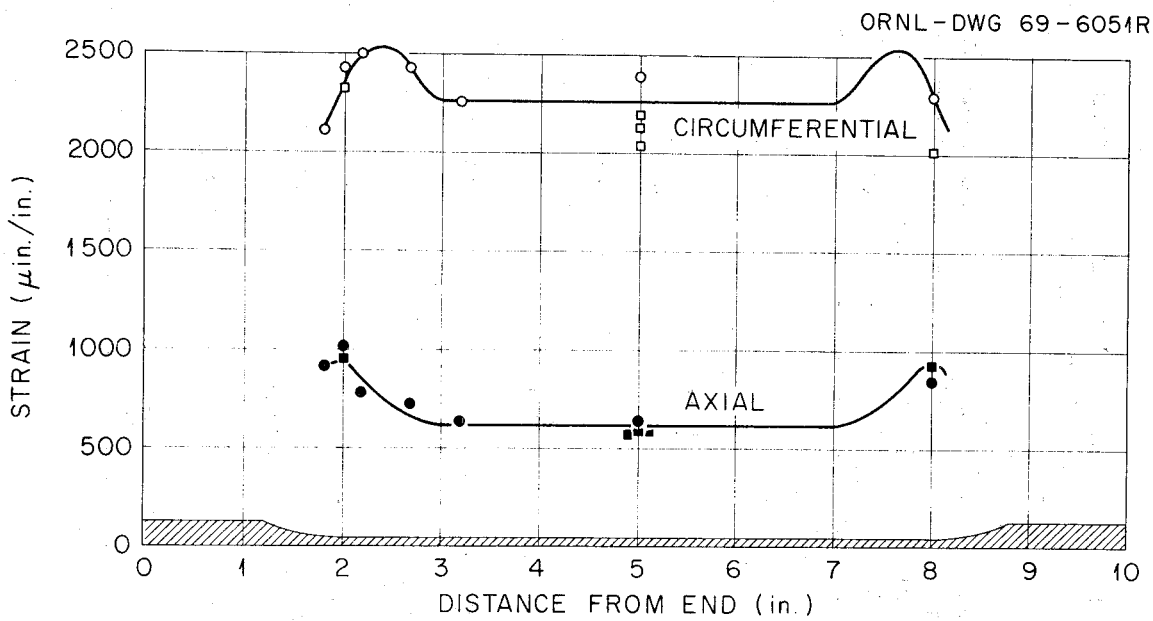

Fig. 4. Strain distribution in Graphitite-G tube no. 3 under 200 psi internal pressure.

loading. The strain values from gages along a single generator are shown as circles. The strains for other gage locations around the circumference of the specimen are denoted by squares.

Twenty-four tensile specimens were used to obtain stress versus longitudinal strain and stress versus lateral strain data. Eight with-grain and eight against-grain specimens were machined from 2-in.-diam rod stock, while eight additional against-grain specimens were machined from the tube stock, which had a 2 in. inside diameter and a 2 3/4 in. outside diameter. The latter stock was also used to make end sleeves for the thin-walled cylindrical specimens. A modified ASTM specimen design[11] was used in each case. Figure 5 shows the design of the with-grain specimen; the gage section was 0.310 in. in diameter and 3/4 in. in length. The design of the against-grain specimen is shown in Fig. 6, where the specimen is shown superposed on the rod stock cross section. All of the against-grain specimens had a 0.125-in.-diam, 1/2-in.-long gage section. In the case of the specimens from tube stock, cylindrical rods and end caps, as shown in Fig. 7(A), were made and assembled to form a composite structure. This structure was then machined to the final configuration illustrated in Fig. 7(B).

Each against-grain specimen was instrumented with four Micro-Measurement type MA-13-050AH-120 strain gages with a 0.050-in. gage length. Two of the gages were oriented in the axial direction and two were oriented in the circumferential direction. The two axial gages were located 180-deg apart. The circumferential gages were mounted to form T configurations with the axial gages. Each with-grain specimen was similarly instrumented with four type C6-111 Budd Metalfilm strain gages having a 0.063-in. gage length.

Since the parameters, or constants, in the constitutive equations cannot be determined from monotonic loading alone, the specimens were generally cycled twice between zero and a constant maximum stress level before being loaded to failure. Two of the with-grain specimens and one against-grain specimen were loaded to failure without cycling, while one with-grain specimen was cycled between zero and 3600 psi prior to being loaded to failure. The remaining five with-grain specimens were cycled

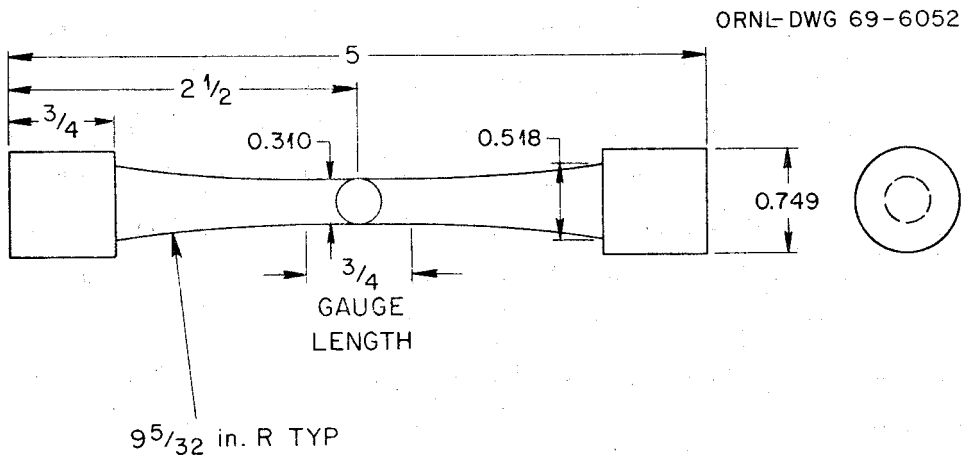

DIMENSIONS ARE IN INCHES

Fig. 5. With-grain tensile specimen.

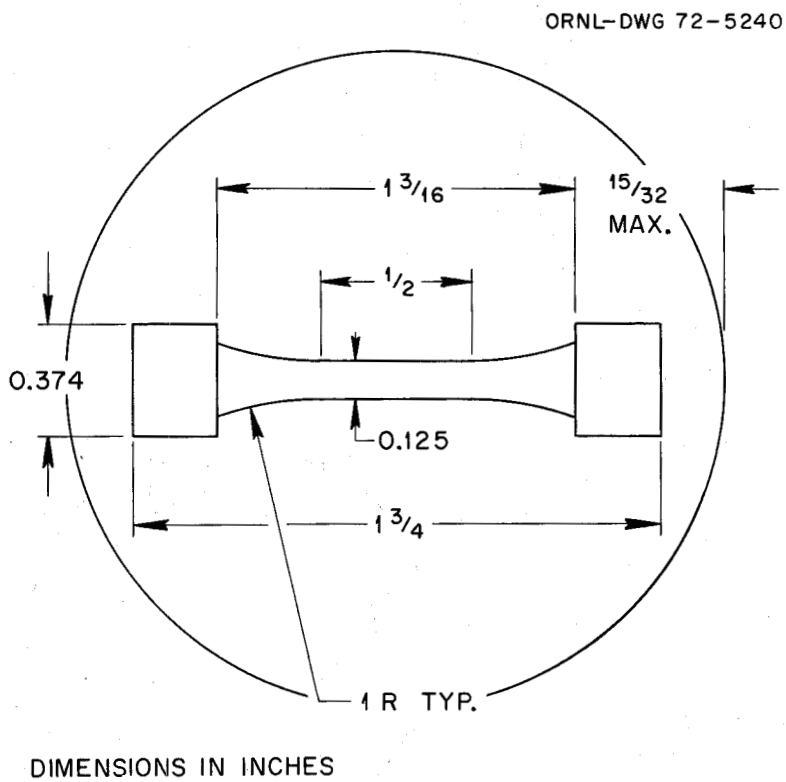

Fig. 6. Against-grain tensile specimen.

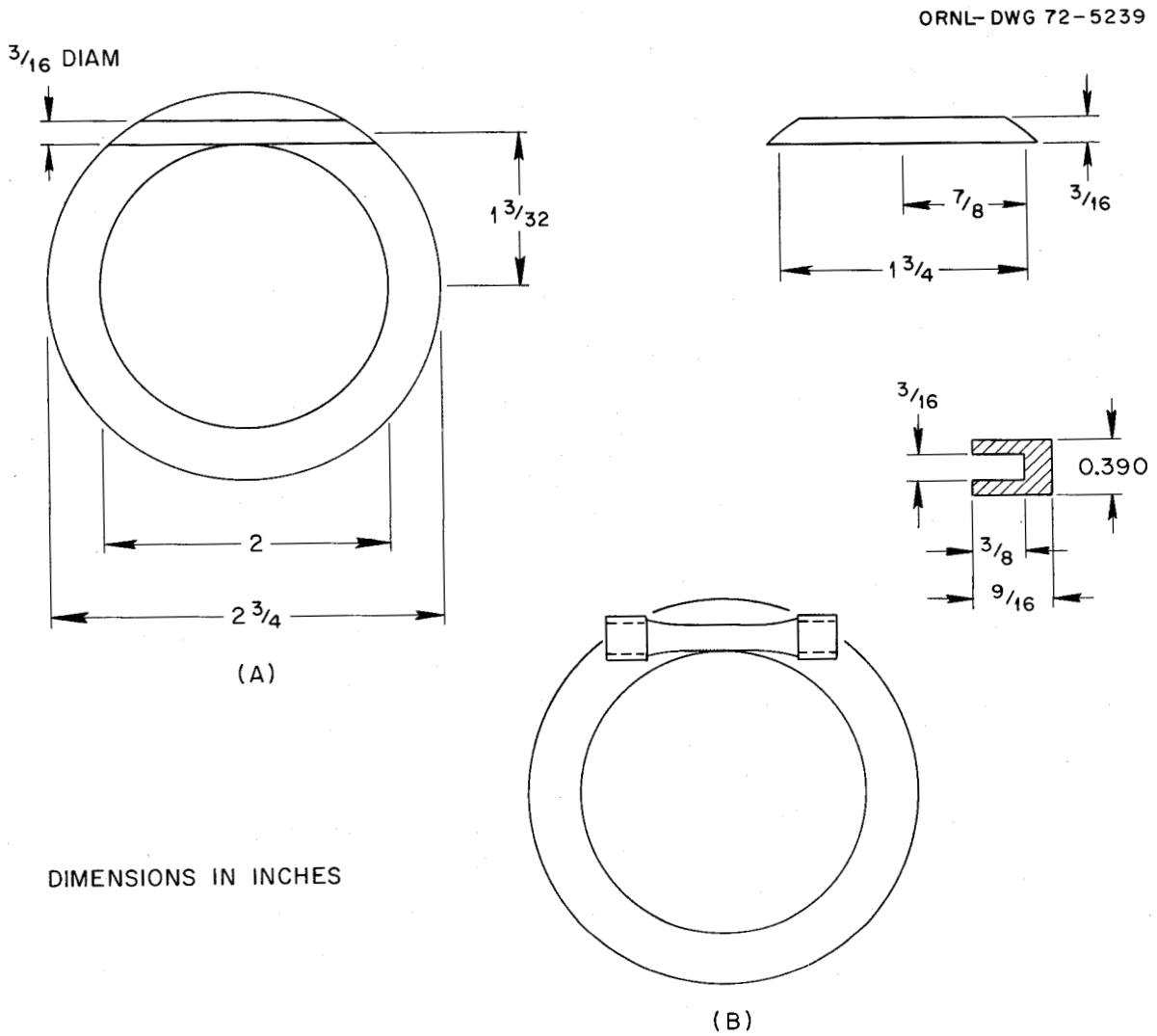

Fig. 7. Details of against-grain tensile specimen from tube stock.

between zero and 1800 psi as were all of the against-grain specimens, except the one just mentioned.

A typical stress versus longitudinal strain diagram is shown in Fig. 8. This diagram is for an against-grain specimen that was made from rod stock and cycled twice before loading to failure. The envelope for all stress-strain curves (ignoring the unloading and reloading, or cyclic, portions), the mean of these curves, and the fracture points for the against-grain specimens are shown in Fig. 9. The circled fracture point is that for the specimen which was failed without cycling.

The corresponding stress-strain curve envelope and mean curve as well as the fracture points for the eight with-grain specimens are shown in Fig. 10. The circled fracture points are those for the two specimens which were loaded to failure without cycling, and the square designates the fracture point for the specimen which was cycled between zero and 3600 psi. These figures show that the scatter in data is not large so far as graphite is concerned and that cycling had no apparent influence on failure.

TEST RESULTS, GRAPHITITE-G MATERIAL

The stress-strain curves from the against-grain and with-grain uniaxial specimens were used to determine the parameters in Eqs. (9), (10), and (11). These include the elastic moduli, the material constants which characterize the plastic deformations, and the constant c. Lateral-to-longitudinal strain ratio, or total strain ratio, data were also obtained. The total strain ratios were then decomposed into elastic and plastic components through the use of the following equation:[12]

$$\bar{\mu} = \frac{\nu\epsilon^{e} + \mu^{p}\epsilon^{p}}{\epsilon} , \qquad (27)$$

where

$\bar{\mu}$ = total, or apparent, strain ratio,

ϵ = longitudinal strain $(= \epsilon^{e} + \epsilon^{p})$,

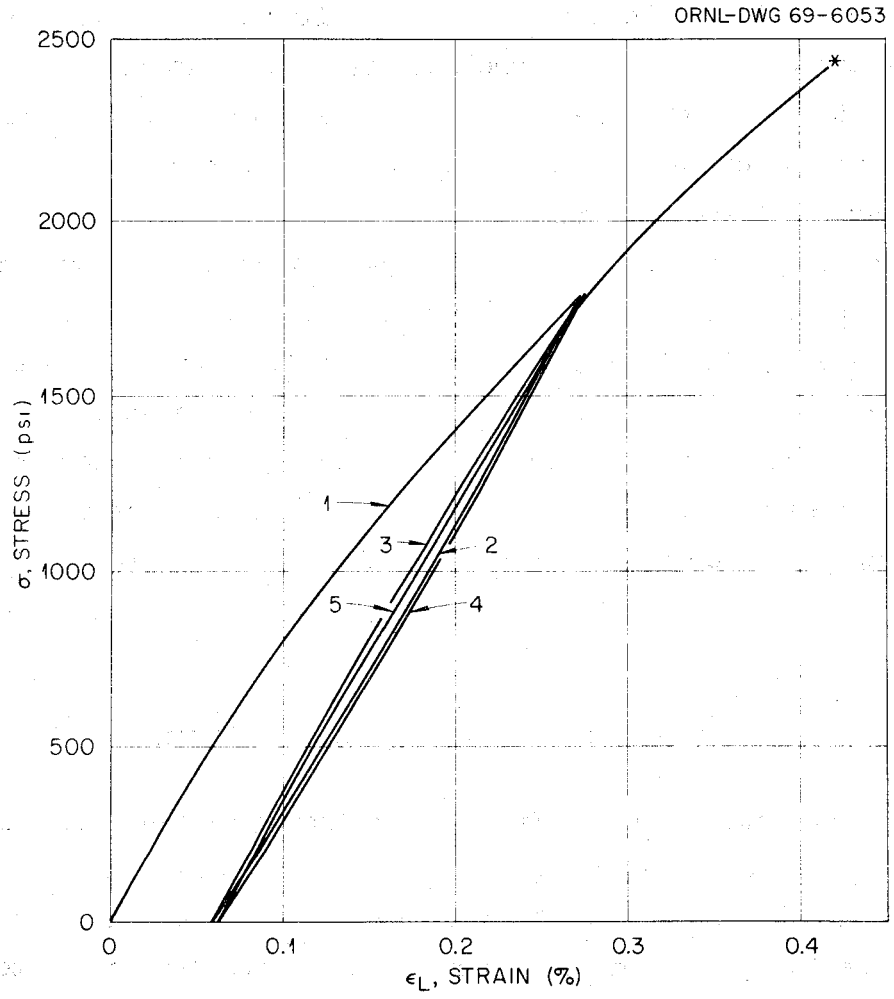

Fig. 8. Stress vs longitudinal strain diagram for against-grain specimen.

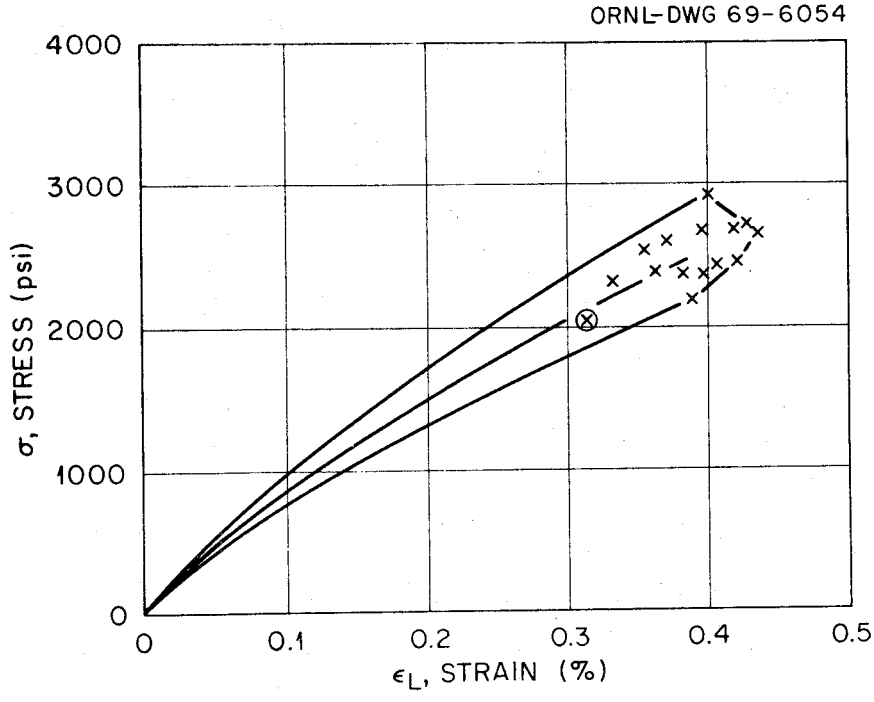

Fig. 9. Against-grain tensile data.

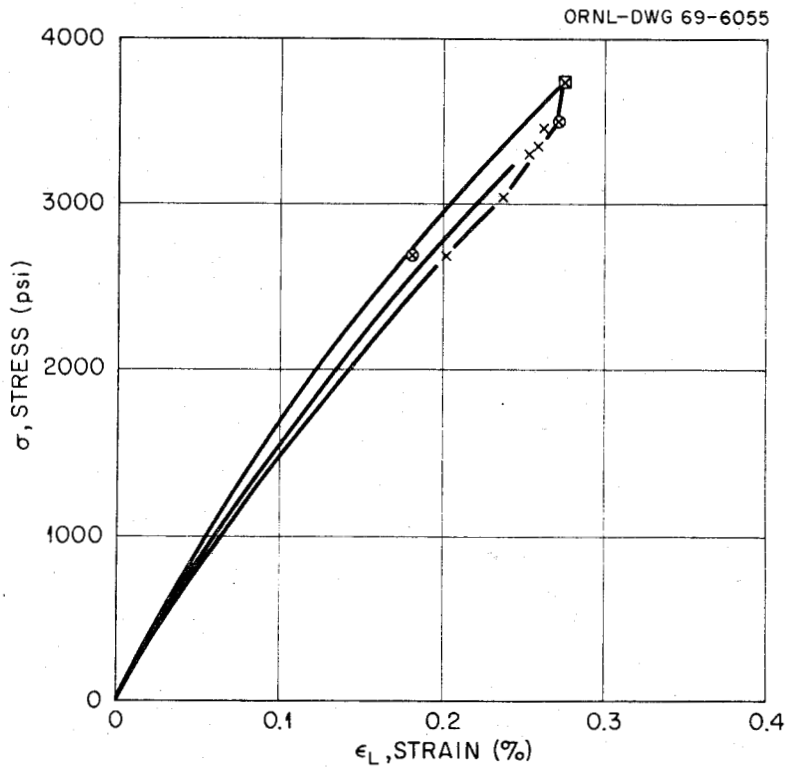

Fig. 10. With-grain tensile data.

ν = Poisson's ratio, strain ratio in the limit of zero stress, or strain,

μ^p = plastic strain ratio.

The elastic modulus, $E(=E_{11}=E_{22})$, and plastic constant, $B(=B_{11})$, as determined from the initial loading curves, are listed in Table 2 for each of the 15 against-grain specimens that were cyclically loaded. The method used for making these determinations is described in Ref. 8. Also given are averages of the E and cB values which were determined from the first unloading, first reloading, and second unloading portions of the cyclic curves (see Fig. 8). The average value of E is 1.08×10^6 psi for initial loading, while this value as determined from the unloading and reloading curves is 1.01×10^6 psi. Thus, the two average values are in good agreement. The average value for B is 272×10^{-12} psi^{-2}, and that for cB is 67×10^{-12} psi^{-2}, giving a value for c of 0.25 which differs significantly from the value of one-half which was given by Jenkins.[4]

The corresponding results for the six with-grain specimens that were cyclically loaded are given in Table 3. The results from the two specimens which were loaded to failure without being cycled are not included. In the case of these data, the average value for $E(=E_{33})$, as determined from the initial loading curves, is 1.86×10^6 psi, and that from the unloading and reloading curves is 1.96×10^6 psi. The latter is somewhat higher than the former, while in the case of the against-grain specimens the reverse is true. However, the agreement between the two values is again good. The average $B(=B_{33})$ value is 73×10^{-12} psi^{-2}, and the average value for cB is 26×10^{-12} psi^{-2}. Thus, the value for c is 0.36, which again is significantly different from one-half. Because c is assumed to be a constant that is independent of the orientation of the specimen, the average of the two values, or 0.30, will be used in the analysis described in this report.

The average total strain-ratio curve, which is designated by $\bar{\mu}_{31}$ in Fig. 11, was obtained from seven with-grain specimens. Since the elastic strain ratio is equal to the total strain ratio in the limit of zero longitudinal strain, ν_{31} is represented by the straight line parallel to the longitudinal strain axis in this figure. Equation (27) was used to calculate the curve for the plastic strain ratio, μ^p_{31}. In this case, μ^p_{31}

Table 2. Graphitite-G against-grain tensile data

Specimen no.	Initial loading		Unloading and reloading		Stock material
	E (10^6 psi)	B (10^{-12} psi^{-2})	E_{ave} (10^6 psi)	$(cB)_{ave}$ (10^{-12} psi^{-2})	
R1	1.13	277	1.01	71	Rod stock: 2-in.-diam
R2	1.02	288	0.96	78	
R3	1.07	334	0.93	76	
R4[a]			0.92	64	
R5	0.98	364	0.93	85	
R6	0.99	298	0.95	80	
R7	1.04	284	0.95	75	
R8	1.14	268	1.02	60	
Average:	1.05	302	0.96	74	
T1	1.05	290	0.97	54	Tube stock: 2-in.-ID × 2 3/4-in.-OD
T2	1.11	281	1.02	63	
T3	1.10	268	1.04	72	
T4	1.14	225	1.09	61	
T5	1.15	230	1.10	55	
T6	1.10	220	1.08	63	
T7	1.16	175	1.13	51	
Average:	1.11	241	1.06	60	
Average for combination of rod and tube specimens:					
	1.08	272	1.01	67	

[a]The initial loading portion of the curve obtained was not suitable for evaluating the constants. The results from this specimen are not included in Fig. 9.

Table 3. Graphitite-G with-grain tensile data

Specimen no.	Initial loading		Unloading and reloading		Stock material
	E (10^6 psi)	B (10^{-12} psi^{-2})	E_{ave} (10^6 psi)	$(cB)_{ave}$ (10^{-12} psi^{-2})	
R1	1.93	55	1.84	17	Rod stock: 2-in.-diam
R2	1.87	77	2.04	31	
R3	1.78	76	1.88	17	
R4	1.88	73	2.09	39	
R5	1.90	87	1.97	25	
R6	1.80	72	1.91	28	
Average:	1.86	73	1.96	26	

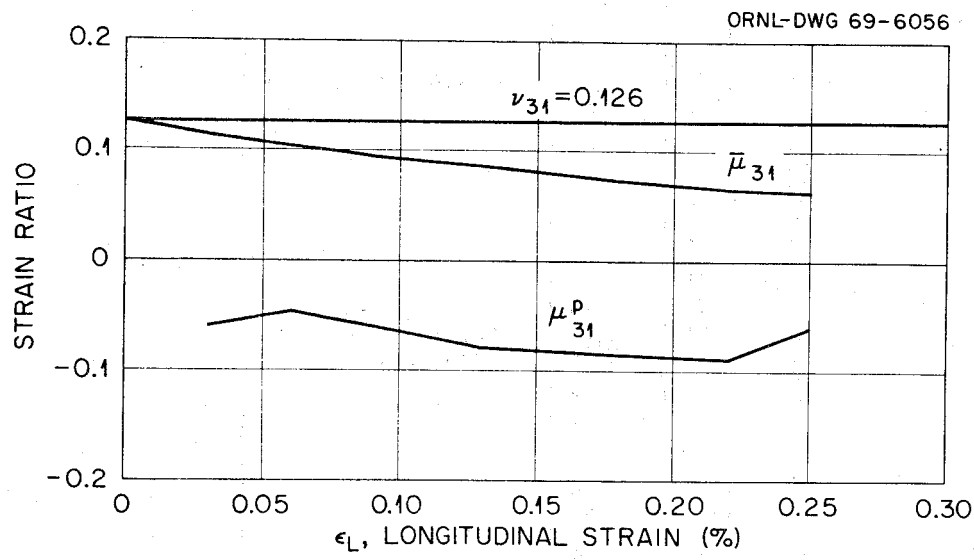

Fig. 11. Average strain-ratio data for seven Graphitite-G with-grain tensile specimens.

is essentially independent of the longitudinal strain and it is negative in the range shown. However, the apparent strain-ratio data lack precision in the small strain range shown, and additional inaccuracies are introduced in the decomposition process. Hence, the value of μ_{31}^{p} can be assumed constant without introducing significant error. By giving greater weight to the values at larger longitudinal strains, a value of −0.08 was selected for the purposes here.

The total strain ratios, $\bar{\mu}_{12}$, were determined from three against-grain specimens, and values for ν_{12} and μ_{12}^{p} were obtained in the same manner as the ν_{31} and μ_{31}^{p} values discussed above. These are listed in Table 4 where it can be seen that there are significant differences between the numbers for the three specimens. However, the plastic strain ratio is negative in each case. The average value for ν_{12} from the three specimens is 0.20, while that for μ_{12}^{p} is −0.15.

Since the strain ratios needed in Eqs. (23) through (26) are ν_{13} and μ_{13}^{p}, these quantities were calculated from the above values for ν_{31} and μ_{31}^{p}. Equations (21) give the following relationship between the elastic strain ratios:

$$\nu_{13} = \frac{E_{11}}{E_{33}} \nu_{31} , \tag{28}$$

and Eqs. (22) give the following relationship between the plastic strain ratios:

$$\mu_{13}^{p} = \left(\frac{B_{33}}{B_{11}}\right)^{2/3} \mu_{31}^{p} . \tag{29}$$

Table 4. Graphitite-G strain-ratio data from against-grain tensile specimens

Specimen no.	ν_{12}	μ_{12}^{p}
R7	0.20	−0.13
R8	0.26	−0.28
T3	0.14	−0.05

The values thus determined for ν_{13} and μ_{13}^{p} are 0.07 and −0.03, respectively.

Although s_{KL} and a_{KL} values, as required in Eqs. (23) through (26), were determined from the tensile specimens, variations in material properties preclude their use in making definitive comparisons between calculated and experimental results for the cylindrical specimens under internal pressure loading. The strain-ratio values and the value for c will be used, however. The uniaxial tests conducted on each cylindrical specimen provided means whereby the masking effects due to material variability could be overcome. But it was necessary to determine the needed data in such a way that the effects of prior loading histories did not influence the values obtained.

After loading a specimen in a given direction in stress space,* the stress-strain response obtained upon loading in a different direction is not the same as loading a virgin specimen in the second direction. However, the model of graphite behavior given in Refs. 1 and 2 predicts that, once the specimen has been loaded to a given stress level in the new direction, unloading and reloading curves subsequently obtained by cycling between

$$0 \leq \sigma_{KL} \leq \sigma_{KL}^{*} ,$$

where σ_{KL}^{*} is the stress at the unloading point, are the same as the unloading and reloading curves that would have been obtained using a virgin specimen. Therefore, A and cB values for each of the cylindrical specimens were obtained from cyclic unloading and reloading curves produced by the application and release of an axial force and by cyclic pressurization with no net end load. The B values were then calculated using the value for c from the tensile tests. The average A and B values obtained in this manner are listed for each of the five cylindrical specimens in Table 5. The overall averages for the cylindrical and tensile specimens are given at the bottom of the table.

---

*In this case we are concerned with a two-dimensional space in which the axes are labeled by σ_2 and σ_3, that is, the axial and circumferential stress components, respectively, and we further restrict ourselves to loadings for which the ratio of σ_2 to σ_3 remains constant during a given loading.

Table 5. Data from cylindrical specimens

Specimen no.	A_{11} (10^{-6} psi^{-1})	A_{33} (10^{-6} psi^{-1})	B_{11} (10^{-12} psi^{-2})	B_{33} (10^{-12} psi^{-2})
1	0.73	0.56	123	42
2	0.78	0.47	133	39
3	0.80	0.58	148	50
4	0.76	0.46	136	40
5	0.77	0.55	135	51
Averages:				
Cylinder data	0.78	0.52	138	45
Tensile data	0.92	0.54	272	73

A comparison of the results in Table 5 with those of Tables 2 and 3 shows that, in general, the A and B values are larger for the tensile specimens. Also, Table 2 indicates that the B values for specimens made from rod stock are higher than those from the tube stock, but the value for c is essentially the same for the two cases. Finally, it may be seen that the variations in B values for the cylindrical specimens are less than those for the tensile specimens.

Since strain ratios for metals and other materials are positive, a question naturally arises regarding the validity of the stress-plastic strain relations for the case where negative plastic-strain ratios exist. The validity in the case at hand is determined through an examination of the plastic potential function, which in the mathematical theory of plasticity must represent a convex surface in stress space.[13,14] Therefore, a statement of the requirements for convexity of surfaces given by Eq. (20) is necessary.

Convexity is assured by requiring that the matrix of coefficients,

$$||a_{KL}|| ,$$

be positive definite. The nonzero coefficients in this matrix and the equivalences in terms of measured quantities are given by Eqs. (22). By imposing the positive definite requirement, the following inequalities are obtained:[15,16]

$$\begin{aligned} &B_{11} > 0 , \\ &B_{33} > 0 , \\ &B_{44} > 0 , \\ &-1 < \mu_{12}^{p} < 1 , \\ &(1 - \mu_{12}^{p}) > 2\mu_{13}^{p}\mu_{31}^{p} . \end{aligned} \tag{30}$$

These inequalities show that the strain ratios can be positive or negative so long as they remain within the bounds given. The B values are greater than zero in all cases. Further, it may be seen that the fourth

and fifth inequalities are satisfied. Thus, the surfaces described by Eq. (20) are convex.

COMPARISONS OF CALCULATED AND EXPERIMENTAL RESULTS

The axial and circumferential strains for cylindrical specimens nos. 1 and 2 under the initial internal pressure loading cycles were calculated using Eqs. (23) through (26), the constants in Table 5, and the strain ratios and c value from the tests on tensile specimens. The experimentally determined curves for these specimens are shown in Figs. 12 and 13 where the points calculated from the equations are indicated by the open circles. The experimental and theoretical results shown are in excellent agreement. Similar agreement was found for the remaining specimens.

Figure 14 shows the comparisons between theoretical and experimental results representing the averages from specimens nos. 2 through 5 when the A and B values obtained from these cylindrical specimens are used. Again, the figure shows that the results are in excellent agreement.

The results of the studies given in this report demonstrate the need for determining uniaxial data directly from the specimens tested under combined states of stress. However, investigations using other graphites have shown that very good agreement between calculated and experimental results for graphites exhibiting small variations in mechanical properties are obtained when data from tensile specimens alone are used in the analyses. Thus, for some graphites, the precautions taken here in obtaining materials properties data are not necessary, and the equations may be used with confidence for practical applications when stress-strain data from the uniaxial specimens alone are obtained.

To illustrate this point, a comparison between calculated and experimental results for a specimen made from a specialty graphite are shown in Fig. 15. The parameters used in the constitutive equations were:

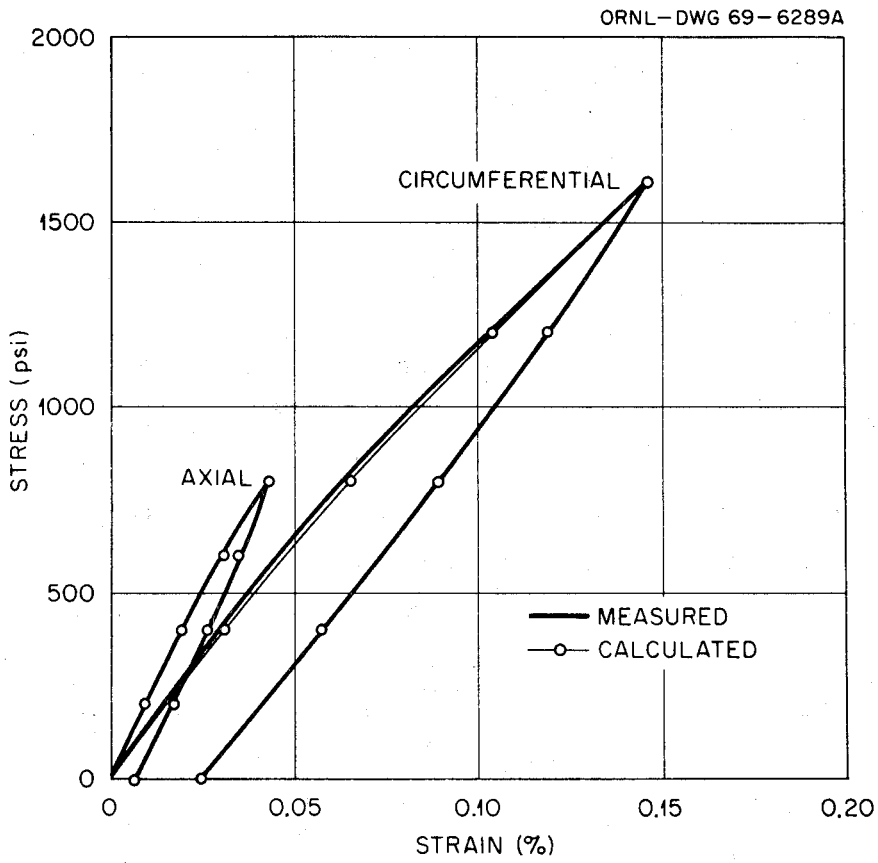

Fig. 12. Comparisons of measured curves with calculated results for Graphitite-G specimen no. 1.

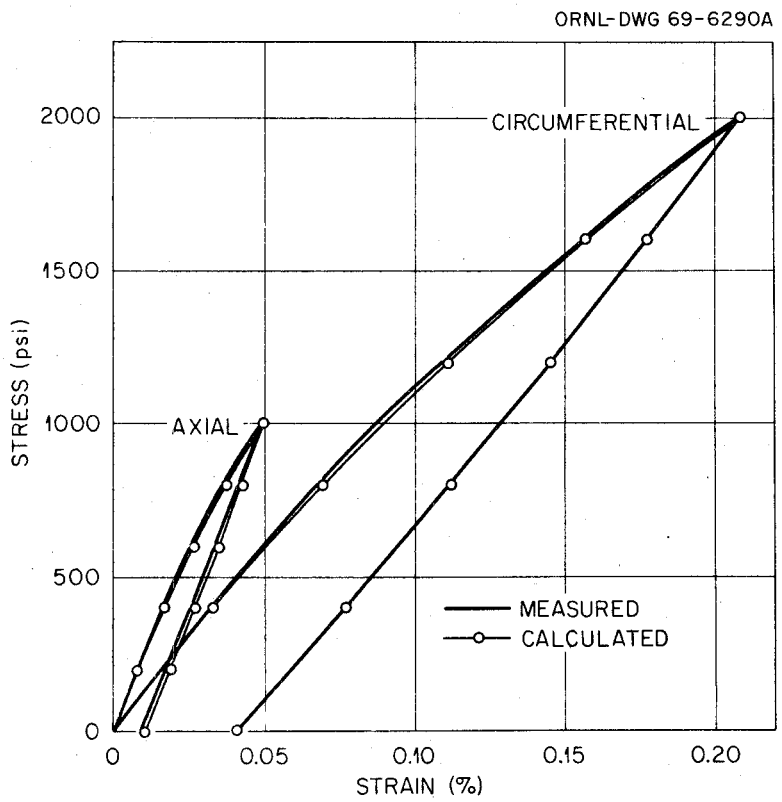

Fig. 13. Comparisons of measured curves with calculated results for Graphitite-G specimen no. 2.

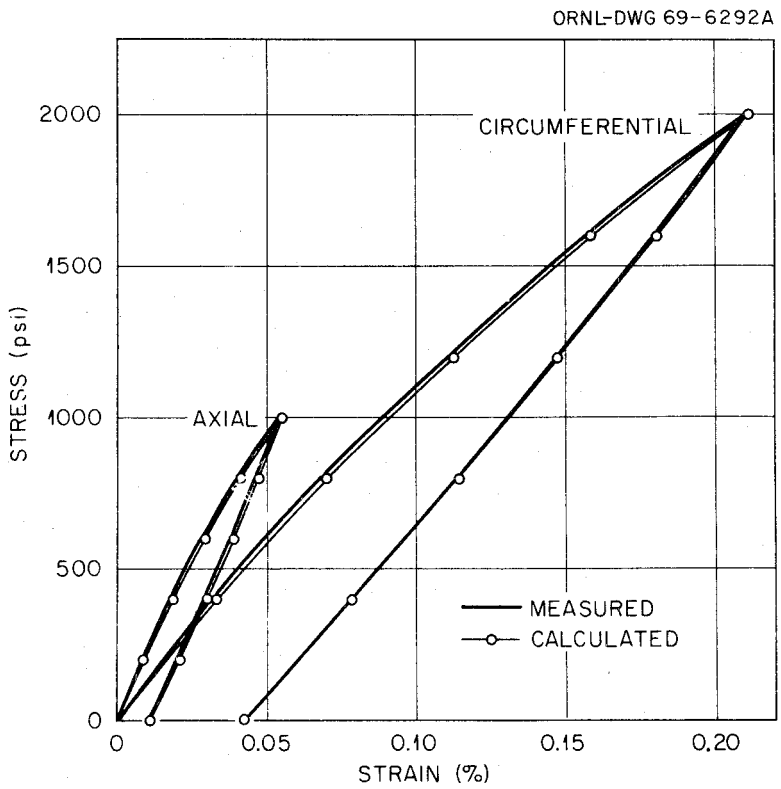

Fig. 14. Comparisons of averaged measured curves and averaged calculated results for Graphitite-G specimen nos. 2 through 5.

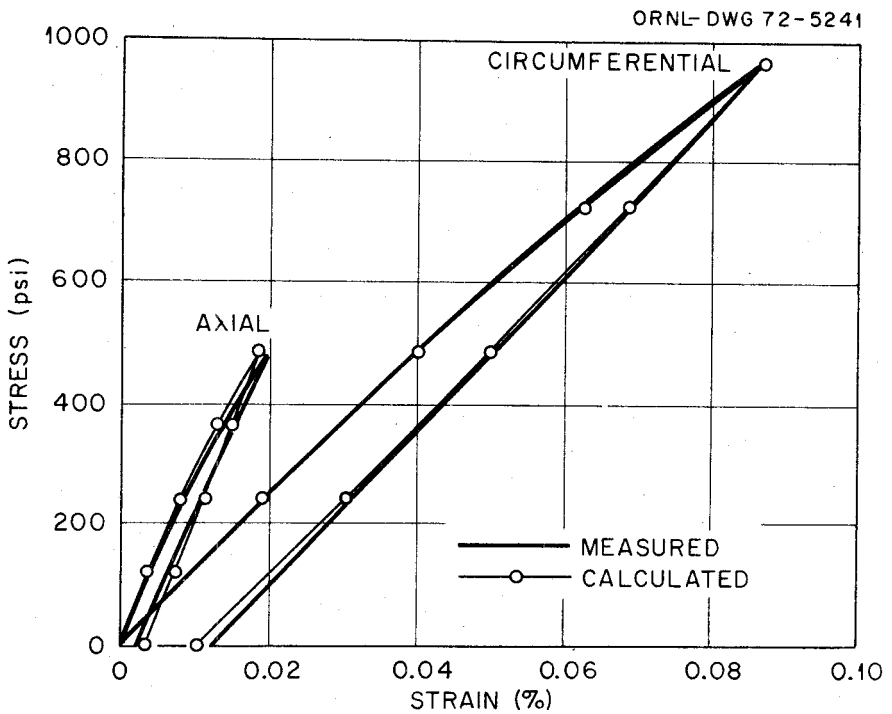

Fig. 15. Comparison of measured curves with calculated results for a specialty graphite.

$E_{11} = 1.27 \times 10^6$ psi $\qquad B_{11} = 99 \times 10^{-12}$ psi^{-2}

$E_{33} = 2.37 \times 10^6$ psi $\qquad B_{33} = 36 \times 10^{-12}$ psi^{-2}

$\nu_{13} = 0.06$ $\qquad \mu_{13}^{p} = -0.10$

$c = 0.25$

where all of the values were determined directly from tests on uniaxial specimens. Again, the agreement between theory and experiment is very good.

CONCLUSIONS

It is shown that nonlinear stress-strain behavior of graphite under combined stress conditions at room temperature can be accurately described by a small-deformation elastic-plastic continuum theory. Results calculated through the use of special constitutive equations appropriate to the description of graphite behavior were shown to be in excellent agreement with experimental results corresponding to initial loading and to unloading under combined states of stress produced by internal pressure in thin-walled cylindrical specimens. Further, the calculated residual strains upon unloading were very close to those determined experimentally.

In the examination of a theory, such as that described, it is essential that experiments be designed to overcome problems associated with the accurate determination of material constants and to minimize masking effects due to material variability. Because of the variability in mechanical behavior of the primary material used, parameters for use in the constitutive equations in this investigation were determined using results from tensile specimens along with uniaxial data obtained from the thin-walled cylindrical specimens. The results derived establish, in part, the validity of the theory. Additional investigations to examine this theory should be designed to study the basic postulates since the validity has been established, as shown here, in what may be considered a gross sense.

ACKNOWLEDGMENTS

The authors gratefully acknowledge the assistance of H. A. MacColl in the data reduction, and J. M. Chapman for his help in instrumenting and testing the specimens.

REFERENCES

1. W. L. Greenstreet, "Constitutive Equations for Artificial Graphite," Ph.D. dissertation, Yale University, June 1968.

2. W. L. Greenstreet and A. Phillips, "A Theory of an Elastic-Plastic Continuum with Special Emphasis to Artificial Graphite," Acta Mechanica (to be published).

3. W. L. Greenstreet and A. Phillips, "An Elastic-Plastic Theory for Artificial Graphite," Proceedings of the First International Conference on Structural Mechanics in Reactor Technology (to be published).

4. G. M. Jenkins, Brit. J. Appl. Phys., 13: 30 (1962).

5. G. M. Jenkins and G. K. Williamson, J. Appl. Phys., 14(9): 2837 (1963).

6. J. Rappeneau, C. Jouquet, and M. Guimard, Carbon, 3: 407 (1966).

7. E. J. Seldin, Carbon, 4: 177 (1966).

8. W. L. Greenstreet, J. E. Smith, and G. T. Yahr, Carbon, 7: 15 (1969).

9. A. E. H. Love, A Treatise on the Mathematical Theory of Elasticity, Dover, 4th ed., New York, 1944.

10. R. F. S. Hearmon, An Introduction to Applied Anisotropic Elasticity, Oxford University Press, London, 1961.

11. "Standard Methods of Tension Testing of Carbon-Graphite Mechanical Materials," ASTM Designation: C565-71, pp. 496-499 in 1971 Annual Book of ASTM Standards, Part 13, American Society for Testing and Materials, Philadelphia, 1971.

12. F. R. Shanley, Weight-Strength Analysis of Aircraft Structures, Dover, 2nd ed., New York, 1960.

13. W. Prager, "Recent Developments in the Mathematical Theory of Plasticity," J. Appl. Phys., 20: 235 (1949).

14. D. C. Drucker, "A More Fundamental Approach to Plastic Stress-Strain Relations," pp. 487-491 in Proceedings of the First U.S. National Congress of Applied Mechanics, New York, 1952.

15. F. M. Stein, Introduction to Matrices and Determinants, Wadsworth Publishing Co., Belmont, California, 1967, pp. 100-101.

16. M. Born and K. Huang, Dynamical Theory of Crystal Lattices, Clarendon Press, Oxford, 1954, p. 141.

Internal Distribution

1. S. E. Beall
2. H. W. Behrman
3. S. E. Bolt
4. J. W. Bryson
5. J. P. Callahan
6. S. J. Chang
7. J. L. Cook (Y-12)
8. W. H. Cook
9. J. M. Corum
10. W. B. Cottrell
11. F. L. Culler
12. W. G. Dodge
13. W. P. Eatherly
14. A. P. Fraas
15. J. M. Googin (Y-12)
16-20. W. L. Greenstreet
21. R. C. Gwaltney
22. P. N. Haubenreich
23. H. W. Hoffman
24-70. P. R. Kasten
71. C. R. Kennedy
72. K. C. Liu
73. M. I. Lundin
74. R. N. Lyon
75. R. E. MacPherson
76. H. C. McCurdy
77. G. B. Marrow (Y-12)
78. J. G. Merkle
79. A. J. Miller
80. S. E. Moore
81. J. M. Napier (Y-12)
82. A. M. Perry
83. C. E. Pugh
84. M. W. Rosenthal
85. Myrtleen Sheldon
86. M. J. Skinner
87. J. E. Smith
88. I. Spiewak
89. D. A. Sundberg
90. D. B. Trauger
91-95. R. S. Valachovic
96. G. D. Whitman
97-101. G. T. Yahr
102-103. Central Research Library
104. Y-12 Document Reference Section
105-109. Laboratory Records Department
110. Laboratory Records (RC)

External Distribution

111. Leopold Albertin, Westinghouse Astronuclear Lab., Large, Penna. 15236
112. R. W. Andrae, Los Alamos Scientific Lab., Los Alamos, N.M. 87544
113. P. E. Armstrong, Los Alamos Scientific Lab., Los Alamos, N.M. 87544
114. I. Auerbach, Sandia Laboratories, Albuquerque, N.M. 87115
115. S. G. Babcock, General Motors Technical Center, Warren, Mich. 48089
116. B. L. Bailey, Great Lakes Carbon Corp., Niagara Falls, N.Y. 14302
117. R. A. Baker, Sandia Laboratories, Albuquerque, N.M. 87115
118. R. D. Baker, Los Alamos Scientific Lab., Los Alamos, N.M. 87544
119. W. T. Barry, Aerospace Corp., El Segundo, Calif. 90245
120. M. Baud, Great Lakes Research Corp., Elizabethton, Tenn. 37643
121. C. W. Bert, Sandia Laboratories, Albuquerque, N.M. 87115
122. J. H. Biffle, Sandia Laboratories, Albuquerque, N.M. 87115
123. D. E. Bishop, Sandia Laboratories, Albuquerque, N.M. 87115
124. J. R. Bohn, TRW Systems, Redondo Beach, Calif. 90278
125. Richard Bolton, Westinghouse Astronuclear Lab., Pittsburgh, Penna. 15236
126. S. A. Bortz, IIT Research Institute, Chicago, Ill. 60616
127. S. W. Bradstreet, 42 Lookout Drive, Dayton, Ohio 45409
128. W. G. Bradshaw, Lockheed Missiles and Space Co., Palo Alto, Calif. 94304

129. L. J. Broutman, Illinois Inst. of Tech., Chicago, Ill. 60616
130. J. D. Buch, Aerospace Corp., Los Angeles, Calif. 90045
131. O. J. Burchett, Sandia Laboratories, Albuquerque, N.M. 87115
132. M. B. Carter, Union Carbide Corp., Cleveland, Ohio 44101
133-134. E. G. Cass, Director, Division of Reactor Standards, U.S. Atomic Energy Commission, Washington, D.C. 20545
135. T. Y. Chang, The Univ. of Akron, Akron, Ohio 44304
136. S. L. Channon, Aerospace Corp., San Bernardino, Calif. 92400
137. William Chard, Pfizer, Inc., Easton, Penna. 18042
138. H. R. W. Cobb, Gulf General Atomic, San Diego, Calif. 92111
139. W. Connell, General Electric Co., Philadelphia, Penna. 19101
140. L. C. Corrington, NASA Lewis Research Center, Cleveland, Ohio 44135
141. J. G. Crose, Aerospace Corp., San Bernardino, Calif. 92400
142. P. N. Dalenburg, Wickes Corp., Saginaw, Michigan 48601
143. J. A. DeMastry, Westinghouse Astronuclear Lab., Pittsburgh, Penna. 15236
144. G. J. DeSalvo, Swanson and Associates, Inc., 870 Pine View Drive, Elizabeth, Penna. 15037
145. J. M. Dillahunty, Air Force Materials Laboratory — SAMSO, San Bernardino, Calif. 92409
146. R. B. Dirling, McDonnell-Douglas Astronautics Co., LaJolla, Calif. 92037
147. W. H. Duckworth, Battelle Memorial Inst., Columbus, Ohio 43201
148. D. M. Forney, Air Force Materials Lab. (MAC), Wright-Patterson Air Force Base, Ohio 45433
149. W. E. Duggins, Collier Carbon and Chemical Corp., Los Angeles, Calif. 90060
150. R. J. Edwards, U.S. Naval Ordnance Laboratory — White Oak, Silver Spring, Maryland 20910
151. B. R. Emrich, Air Force Materials Lab., Wright-Patterson Air Force Base, Ohio 45433
152. G. B. Engle, Gulf General Atomic, San Diego, Calif. 92112
153. F. Essenburg, Univ. of Colorado, Boulder, Colorado 80303
154. J. J. Ferritto, POCO Graphite, Inc., Decatur, Texas 76234
155. E. L. Foster, Battelle Memorial Instute, Columbus, Ohio 43201
156. J. E. Fox, U.S. Atomic Energy Commission, Washington, D.C. 20545
157. A. M. Freudenthal, George Washington Univ., Washington, D.C. 20545
158. E. R. Frye, Sandia Laboratories, Albuquerque, N.M. 87115
159. J. J. Gangler, U.S. Atomic Energy Commission, NASA, Washington, D.C. 20545
160. R. P. Gilliam, TRW Systems, Redondo Beach, Calif. 90278
161. R. Goderstad, U.S. Naval Ordnance Lab., Silver Spring, Md. 20910
162. D. C. Goldberg, Westinghouse Astronuclear Lab., Pittsburgh, Penna. 15236
163. A. E. Goldman, Union Carbide Corp., New York, N.Y. 10017
164. W. G. Gottenberg, Univ. of Colorado, Boulder, Colorado 80302
165. S. J. Green, General Motors Technical Center, Warren, Mich. 48089
166. T. R. Guess, Sandia Laboratories, Albuquerque, N.M. 87115
167. J. A. Gum, General Motors Technical Center, Warren, Mich. 48089
168. N. M. Harrington, Philco-Ford, Newport Beach, Calif. 92660

169. H. Hessing, Los Alamos Scientific Lab., Los Alamos, N.M. 87544
170. L. N. Hjelm, U.S. Air Force Materials Laboratory, Los Angeles, Calif. 90045
171. P. A. Hochstein, General Motors Technical Center, Warren, Mich. 48089
172. J. R. Hunter, U.S. Atomic Energy Commission, Washington, D.C. 20545
173. L. H. Jackson, Oak Ridge Operations, Oak Ridge, Tenn. 37830
174. J. Jortner, McDonnell-Douglas Astronautics Co., Huntington Beach, Calif. 92647
175. R. N. Katz, Army Materials and Mechanics Research Center, Watertown, Mass. 02172
176. H. R. Kendig, Carborundum Co., Niagara Falls, N.Y. 14302
177. K. R. King, TRW Systems, Redondo Beach, Calif. 90278
178. P. C. Kochendorfer, Philco-Ford, Newport Beach, Calif. 92660
179. J. R. Koenig, U.S. Air Force Materials Lab., Wright-Patterson Air Force Base, Ohio 45433
180. F. J. Koubek, U.S. Naval Ordnance Lab., Silver Spring, Maryland 20910
181. K. M. Kratsch, McDonnell-Douglas Astronautics Co., LaJolla, Calif. 92037
182. R. Krefeld, Commission of European Communities, 10 Haagstraat-Alkmaar, The Netherlands
183. W. G. Krellner, Stackpole Carbon Co., St. Marys, Penna. 15857
184. R. G. Lawton, Los Alamos Scientific Lab., Los Alamos, N.M. 87544
185. J. J. Lombardo, U. S. Atomic Energy Commission, SNSO, Washington, D.C. 20545
186. V. Lungagnani, Commission of European Communities, 10 Haagstraat-Alkmaar, The Netherlands
187. D. P. MacMillan, Los Alamos Scientific Lab., Los Alamos, N.M. 87544
188. H. G. MacPherson, Univ. of Tennessee, Knoxville, Tenn. 37916
189. V. P. Mamone, Lockheed Missile and Space Co., Sunnyvale, Calif. 94088
190. H. E. Martens, Jet Propulsion Lab., Pasadena, Calif. 91103
191. C. W. Matthews, Sandia Laboratories, Albuquerque, N.M. 87115
192. L. E. McAllister, AVCO Corp., Lowell, Mass. 01851
193. D. D. McBride, Sandia Laboratories, Albuquerque, N.M. 87115
194. T. B. McDonough, General Electric Co., Philadelphia, Penna. 19101
195. J. J. McGahan, Carborundum Co., Grand Island, N.Y. 14072
196. J. R. McGrellis, Union Carbide Corp., Parma, Ohio 44101
197. T. K. McKinley, Aerospace Corp., San Bernardino, Calif. 92402
198. D. F. McVey, Sandia Laboratories, Albuquerque, N.M. 87115
199. J. L. Mershon, U.S. Atomic Energy Commission, Washington, D.C. 20545
200. R. A. Meyer, Aerospace Corp., El Segundo, Calif. 90245
201. R. J. Michalak, General Electric Co., Philadelphia, Penna. 19101
202. W. C. Morgan, Battelle-Northwest Lab., Richland, Wash. 99352
203-205. P. A. Morris, Director, Division of Reactor Licensing, U.S. Atomic Energy Commission, Washington, D.C. 20545
206. R. B. Mortensen, Aerospace Corp., San Bernardino, Calif. 92402
207. C. G. Murphy, Sandia Laboratories, Albuquerque, N.M. 87115

208. W. E. Murr, Westinghouse Astronuclear Lab., Pittsburgh, Penna. 15228
209. D. E. Niesz, Battelle Memorial Institute, Columbus, Ohio 43201
210. E. Olcott, Atlantic Research Corp., Alexandria, Va. 22314
211. N. Olesen, Airco Speer Corp., Niagara Falls, N.Y. 14302
212. E. T. Onat, Yale Univ., New Haven, Conn. 06520
213. R. F. Parisse, AVCO Systems Dov., Wilmington, Mass. 01887
214. S. J. S. Parry, Gulf General Atomic, San Diego, Calif. 92111
215. C. D. Pears, Southern Research Institute, Birmingham, Ala. 35205
216. A. Phillips, Yale Univ., New Haven, Conn. 06520
217. U. A. Pineda, Aerojet-General Corp., Sacramento, Calif. 95813
218. G. A. Pinkas, NASA Lewis Research Center, Cleveland, Ohio 44135
219. J. W. Prados, Univ. of Tennessee, Knoxville, Tenn. 37916
220. C. A. Pratt, U.S. Air Force Materials Laboratory, Wright-Patterson Air Force Base, Ohio 45433
221. R. J. Price, Gulf-General Atomic, San Diego, Calif. 92037
222. L. G. Quan, Lockheed Missiles and Space Co., Sunnyvale, Calif. 94088
223. W. G. Ramke, U.S. Air Force Materials Laboratory, Wright-Patterson Air Force Base, Ohio 45433
224. Y. R. Rashid, General Electric Co., San Jose, Calif. 95125
225. T. A. Redfield, Aerojet-General Corp., Sacramento, Calif. 95813
226. D. J. Rigali, Sandia Laboratories, Albuquerque, N.M. 87544
227. H. C. Roland, Univ. of Tennessee, Knoxville, Tenn. 37916
228. J. C. Rowley, Los Alamos Scientific Lab., Los Alamos, N.M. 87544
229. T. C. Reuther, U.S. Atomic Energy Commission, Washington, D.C. 20545
230. Sennosuke Sato, Ibaraki Univ., 4-12-1 Nakanarusawa Machi, Hitachi, Japan
231. J. T. Schamaun, Sandia Laboratories, Albuquerque, N.M. 87115
232. W. S. Scheib, U.S. Atomic Energy Commission, Washington, D.C. 20545
233. R. W. Schroeder, NASA Lewis Research Center, Cleveland, Ohio 44135
234. J. C. Schutzler, McDonnell-Douglas Astronautics Co., Huntington Beach, Calif. 92647
235. F. C. Schwenk, U.S. Atomic Energy Commission, Washington, D.C. 20545
236. E. J. Seldin, Union Carbide Corp., Cleveland, Ohio 44101
237. R. S. Shemenski, Great Lakes Research Corp., Elizabethton, Tenn. 37643
238. L. F. Simbeck, Airco Speer Corp., St. Marys, Penna. 15857
239. J. M. Simmons, U.S. Atomic Energy Commission, Washington, D.C. 20545
240. F. A. Simonen, Battelle Memorial Institute, Columbus, Ohio 43201
241. E. E. Sinclair, U.S. Atomic Energy Commission, Washington, D.C. 20545
242. R. H. Singleton, Westinghouse Astronuclear Lab., Pittsburgh, Penna. 15236
243. M. C. Smith, Los Alamos Scientific Lab., Los Alamos, N.M. 87544
244. R. D. Snyder, West Virginia Univ., Morgantown, W. Va. 26106
245. W. J. Spry, Carborundum Co., Niagara Falls, N.Y. 14302
246. P. A. Stancampanio, Westinghouse Astronuclear Lab., Pittsburgh, Penna. 15236
247. O. M. Stanfield, Gulf General Atomic, San Diego, Calif. 92112
248. H. S. Starrett, Southern Research Inst., Birmingham, Ala. 35205
249. D. W. Stevens, Gulf General Atomic, San Diego, Calif. 92112
250. G. C. Stoker, Sandia Laboratories, Albuquerque, N.M. 87115
251. H. M. Stoller, Sandia Laboratories, Albuquerque, N.M. 87115
252. A. M. Strauss, Univ. of Cincinnati, Cincinnati, Ohio 45221

253. R. D. Teter, Lockheed Missiles and Space Co., Sunnyvale, Calif. 94087
254. N. R. Thielke, NASA Lewis Research Center, Cleveland, Ohio 44135
255. H. N. Townsend, Union Carbide Corp., New York, N.Y. 10017
256. O. Vohler, Sigri Elektrographit, Gesellschaft mit beschränkter Haftung, 8901 Meitingen bei Augsburg, Federal Republic of Germany
257. B. C. Wei, U.S. Atomic Energy Commission, Washington, D.C. 20545
258. F. C. Weiler, 744 Holbrook Place, Sunnyvale, Calif. 94087
259. T.-L. Weng, Union Carbide Corp., Cleveland, Ohio 44101
260. M. P. Whittaker, Great Lakes Carbon Co., Elizabethton, Tenn. 27643
261. P. P. Zemanick, Westinghouse Astronuclear Lab., Pittsburgh, Penna. 15236
262-263. Technical Information Center, AEC, OR
264. Research and Technical Support Division, ORO
265-281. Manager, Technical Information Center (TIC), Oak Ridge, Tenn. For Transmittal to Members of the ACRS.